

Fractal analysis of atomizing liquid flows

Sébastien Grout ^a, Christophe Dumouchel ^{a,*}, Jean Cousin ^a, Hans Nuglisch ^b

^a UMR 6614-CORIA, Technopole du Madrillet, B.P. 12 Avenue de l'Université, 76801 Saint-Etienne du Rowray Cedex, France

^b SIEMENS VDO Automotive, 1, Avenue Paul Ourliac, B.P. 1149, 31036 Toulouse Cedex 1, France

Received 28 July 2006; received in revised form 26 January 2007

Abstract

The work reported in this paper questions the relevance of using fractal concept to study liquid primary atomization process by characterizing the shape of the continuous liquid flow from the nozzle exit to the end of the atomization process. First, three fractal methods were tested on synthetic images in order to define the best adapted protocol to the objective of the study. It appeared that the Euclidean distance mapping was the best appropriate method. Second, this technique was applied to analyze series of images of atomizing liquid flows obtained for several working conditions. This application demonstrates that atomizing liquid flows are fractal objects and that primary atomization can be reasonably seen as fractal processes. The appropriateness of fractal concept was also demonstrated by the fact that fractal characteristics such as textural or structural fractal dimension and inner cutoff scale are physically representative of the process investigated here. © 2007 Elsevier Ltd. All rights reserved.

Keywords: Primary liquid atomization; Fractal analysis; Image analyzing technique

1. Introduction

Experimental investigations on the distortion and disintegration of liquid flows evolving in a gaseous environment are very much required to improve our knowledge and understanding of liquid spray production. A rapid overview of the literature in this field shows that although the question of liquid flow distortion has been theoretically investigated for the past decades (Sirignano and Mehring, 2000), experimental investigations on primary breakup processes are lacking (Faeth et al., 1995). Primary breakup designates the process of liquid detachment from the liquid flow surface. This process is important because it initiates the atomization process, controls the extend of the continuous liquid flow and provides the initial conditions of the dispersed flow region. Chigier (2005) drew attention to the necessity of studying the breakup region since it is the vital link between liquid emerging from the nozzle and the fully developed spray. According to him, imaging remains the sole technique for obtaining information about liquid sheets and jets emerging from nozzles and their

* Corresponding author. Tel.: +33 2 32 95 36 23; fax: +33 2 32 91 04 85.
E-mail address: Christophe.Dumouchel@coria.fr (C. Dumouchel).

subsequent breakup and efforts must be made to record, analyze and interpret the breakup process. The work reported in this paper intends to participate to this effort.

Regardless the working conditions, a continuous liquid stream (that is the liquid flow attached to the nozzle) that atomizes is a geometric object with a complex boundary. Illustrations of this are available in [Dumouchel \(2005\)](#). The characteristic features of the ligaments and drops that detach from the flow depend on the shape of this object. Thus, the shape of the continuous liquid flow appears to be a relevant characteristic feature of the primary breakup process. In the present work, shapes of atomizing liquid flows are analyzed using the concept of fractal dimension.

The concept of fractal dimension was first introduced by Kolmogorov in its description of small scale turbulence ([Hunt and Vassilicos, 1991](#)) and was then generalized by [Mandelbrot \(1982\)](#). The fractal dimension is an extension of the Euclidean dimension and allows describing complex boundaries. For a straight line, Euclidean and fractal dimensions are equal to 1. For a line inscribed in a plane, the fractal dimension varies from 1 if the line is straight to 2 if the line is so tortuous that it fully covers the whole plane. Fractal dimension is a measure of the tortuosity, fragmentation or roughness of a surface or a line that is self-similar over a range of scales, i.e., that presents similar structures when observed at different magnifications. Fractal analysis is used in different fields of physics and medicine where shapes of objects have to be known. For instance, it is extensively used to characterize neurons and cells morphology ([Caserta et al., 1995](#); [Panico and Sterling, 1995](#); [Smith et al., 1996](#)). In physics, fractal analysis has been widely developed to characterize scalar interface in turbulent flows ([Sreenivasan and Meneveau, 1986](#); [Prasad and Sreenivasan, 1990](#); [Sreenivasan, 1991](#); [Lane-Serff, 1993](#)). A similar application was due to [Chehroudi and Talley \(2004\)](#) to characterize the boundary of a liquid spray under several atmospheric conditions. In combustion, it is used to study the shape of turbulent front flame ([Hall et al., 1992](#)) as well as the morphology of soot particles ([Kaye, 1989](#); [Köylü et al., 1995](#)). Another type of application concerns the characterization of spray surface coatings ([Guessasma et al., 2003](#)). Surprisingly, the application of fractal analysis to study the morphology of atomizing liquid flows has received very little attention. Two approaches must be mentioned.

The first application of fractal analysis to describe the primary breakup process of a liquid flow is due to [Shavit and Chigier \(1995\)](#) who considered the liquid–gas interface of an air assisted cylindrical liquid jet. They found that such an interface is locally fractal and that the average local fractal dimension increases, reaches a maximum and decreases as the distance from the nozzle increases. The local fractal dimension is maximum in the region where the drop production is the most effective. [Shavit and Chigier \(1995\)](#) also reported that the maximum local fractal dimension was related to the breakup length and to an average drop diameter. According to the authors, the fractal nature of the interface of air-assisted liquid jets is a consequence of the interaction of the air turbulence and its eddy structure with the liquid–gas interface.

The relevance of using fractal analysis to characterize an atomization process was confirmed by a second investigation recently published ([Dumouchel et al., 2005b](#)) and that considered liquid streams issuing from low injection pressure simplified cavity nozzles. Contrary to the situations examined by [Shavit and Chigier \(1995\)](#), such atomization processes are characterized by low Weber number revealing the negligible influence of the aerodynamic forces on the atomization process. It was shown that the interface distortion and drop production were initiated by liquid turbulent level and governed by surface tension forces ([Dumouchel et al., 2005a](#)). This second investigation led to similar conclusions as those obtained by [Shavit and Chigier \(1995\)](#).

Fractal analysis may bring another information than the sole fractal dimension. Fractal objects can be divided in two groups: linear (or ideal) fractals and non-linear (or natural) fractals ([Foroutan-pour et al., 1999](#); [Guessasma et al., 2003](#)). Linear (or ideal) fractals result from an absolute generating process and are mathematical objects for which the rule of construction is known. The determination of the fractal dimension is analytical and it can be exactly calculated over a semi-infinite domain. Non-linear (or natural) fractals result from a statistical generating process. Physical objects, as those enumerated above, fall into this category and report fractal property in a range of physical cutoff length scales. In atomization, these cutoffs correspond to the smallest and greatest interface perturbation length scales and constitute interesting characteristics of the primary atomization process ([Shavit and Chigier, 1995](#); [Dumouchel, 2005](#)). However, the determination of these scales is sensitive to the method used to measure the fractal dimension.

The purpose of the present study is to identify the appropriate technique for the fractal analysis of 2D atomizing liquid flow images and to show applications. The next section describes the steps that ought to

be followed in fractal analysis of 2D contours. Section 3 summarizes the experimental visualization technique and the image analyzing process used to elaborate the 2D contours. In Section 4, several fractal analysis methods are tested on images of linear fractals paying attention that these images are similar to those of the liquid flow boundary we want to analyze. These tests will allow a protocol of analysis to be defined. The application of this protocol on the liquid flow images and the results are presented in Section 5.

2. Fractal analysis of 2D contours

The fractal analysis of 2D projection images of 3D objects requires three steps: elaboration of the contour (boundary), elaboration of the Richardson–Mandelbrot plot and the interpretation of this plot.

The elaboration of the contour requires first choosing a technique appropriate to visualize the object as accurately as possible. For mono-phase or reacting flows, light scattering (Mie) or laser induced fluorescence (LIF) techniques can be used (Prasat and Sreenivasan, 1990; Hall et al., 1992; Lane-Serff, 1993 for instance). Hall et al. (1992) reported identical fractal dimension of flame front obtained either by MIE or LIF image analysis. For two-phase flows, like liquid flows in gaseous environment, fractal analysis can be performed on light transmission images (Shavit and Chigier, 1995; Chehroudi and Talley, 2004; Dumouchel et al., 2005b). Whatever the technique used, it must ensure appropriate temporal resolution for the object to be frozen and a good spatial resolution to avoid digitalization effect in the spatial scale range of interest. Because 2D images of 3D objects are used, the “thickness” of the image is an important parameter also. It corresponds to the thickness of the laser sheet or to the depth of field according to the visualization technique. In their study on single phase turbulent flows, Prasat and Sreenivasan (1990) reported an increase of the fractal dimension as the thickness of the laser sheet decreases. Shavit and Chigier (1995) in their analysis of air assisted atomizing jets found that the fractal dimension increases as the image depth of field increases. The influence of the “image thickness” depends on the investigation.

Another parameter to be considered here is the number of images to be treated to have a representative temporal averaging. This number varies from a few tens to a few hundreds according to the study. The minimum number of images to be analyzed may vary from one situation to another and must be determined on the basis of preliminary tests.

Second, the contour must be extracted from the images. Techniques based on the analysis of the gray level histogram are necessary to determine the appropriate threshold that dissociates the object from the background. This step is important especially when the contrast of the image is low. Many experimental investigations reported a non-negligible influence of the threshold on the fractal dimension (Sreenivasan and Meneveau, 1986; Prasat and Sreenivasan, 1990; Sreenivasan, 1991; Hall et al., 1992; Chehroudi and Talley, 2004). They all reported a threshold range in which the fractal dimension is constant. Hall et al. (1992) defined the physical distance corresponding to this range as the fractal thickness and recommended that the contour should lie in this physical zone. However, Prasat and Sreenivasan (1990) found that the range of scale similarity varied with the threshold and was decidedly smaller for intermediate threshold. This behavior was reported by jet longitudinal section analyses and explained as being related to the presence of inhomogeneities in these sections.

The final step before the analysis is the contour plot. Smith et al. (1996) and Foroutan-pour et al. (1999) agree that fractal analysis should be conducted on skeletal images and not on silhouette images. Furthermore, Foroutan-pour et al. recommended that the contour line should be as thin as possible, i.e., it should be a one-pixel line.

The fractal analysis goes through the construction of the Richardson–Mandelbrot plot. In any case, measuring a fractal dimension involves obtaining the slope of a line in a log–log plot (called the Richardson–Mandelbrot plot) this being one manifestation of statistical scale similarity. This plot shows the size of the structuring element, which is different from one technique to another, versus the number of elements needed to describe, cover or recover the all contour. There are several methods to construct the Richardson–Mandelbrot plot. Smith et al. (1996) classified them in two categories: the length methods and the mass method. The length methods include the structured walk method, the box counting method, the dilation method and the Euclidean distance mapping (EDM) method. These techniques, the name of which can change from one work to another, are described and tested in many references (Prasat and Sreenivasan, 1990; Hall

et al., 1992; Smith et al., 1996; Bérubé and Jébrak, 1999; Guessasma et al., 2003; Chehroudi and Talley, 2004). Tested on closed mathematical objects (like the triadic Koch island of different orders), EDM method was reported to be reliable and weakly sensitive to resolution (Hall et al., 1992; Bérubé and Jébrak, 1999; Guessasma et al., 2003). Smith et al. (1996) found that among the length methods, the dilation method was superior. Chehroudi and Talley's results (2004) pointed out that despite fractal dimensions depend on the methods, their behavior is globally not affected by them.

The second category of methods is the mass method (Smith et al., 1996) or cumulative mass method (Caserta et al., 1995) or sandbox method (Panico and Sterling, 1995). Less used than the length methods, this technique is a variant of the box-counting method. The mass method provides more information about the fractal object than the length method. It deals with a quantitative description of the contour and also leads to the concept of lacunarity and multifractals (Smith et al., 1996). Smith et al. (1996) found that the mass method usually reports higher dimensions than length methods whereas, applying the mass method and the box counting method on biological patterns, Panico and Sterling (1995) obtained similar fractal dimensions.

Other parameters influence the Richardson–Mandelbrot plot, like the orientation, size and overall structure of the object. According to the shape of the object, some orientations may accentuate or reduce the digitalization effect. This is particularly the case when the contour shows straight borders (Bérubé and Jébrak, 1999). However, Chehroudi and Talley (2004) noticed that some methods, like EDM, are more isotropic than others. The total surface area of the object must not be too small. Bérubé and Jébrak (1999) recommended that the minimum object area should be 10,000 pixels. As far as the overall structure of the object is concerned, Bérubé and Jébrak (1999) noticed an increase of the fractal dimension when the object morphology is elongated. This aspect is very important and must be taken into consideration when analyzing an object. It reflects the influence of the structural and textural fractal dimensions (Kaye, 1989). The textural fractal dimension characterizes the tortuosity of the border of the object whereas the structural fractal dimension characterizes the overall morphology of the object. These two dimensions characterize the object in different ranges of similarity scales.

The final step in fractal analysis consists in extracting the fractal dimension and the range of similarity scales from the Richardson–Mandelbrot plot. Using the box counting method, Foroutan-pour et al. (1999) suggested a procedure that identifies the two points where a slope change is observed. The fractal dimension can then be calculated by using at least twelve points between these two points. Unfortunately, slope changes in Richardson–Mandelbrot plots are not always easy to detect. Berntson and Stoll (1997), using the same method to plot the Richardson–Mandelbrot graph, determined the fractal dimension with finite scale corrected dimension technique. This technique consists in removing extreme points (one at the time) of the plot until a self-similarity is found (that is a good linearity in the Richardson–Mandelbrot plot) in the remaining spatial scales. Tested on mathematical fractals, this erosion technique was found to considerably improve the determination of the fractal dimension. Other authors (Panico and Sterling, 1995; Guessasma et al., 1999) measured the evolution of the local slope from the smallest to the largest scale covered by the Richardson–Mandelbrot plot. The object is fractal if the local slope sustains a constant value over a spatial scale range from which the inner and outer cutoff scales can be extracted.

It appears from this review that no fractal analysis technique is, a priori, better than any other since the result depends on the method as well as on the quality of the image. Therefore, it is necessary to test several methods on known mathematical fractals in situations that reflect situations of interest. This procedure was the one followed by Hall et al. (1992) for the study of flame front. This is what is done in the present investigation for the case of atomizing liquid flow in a gaseous environment.

3. Elaboration of the liquid flow contours

The experimental configuration used in this work was presented in detail elsewhere (Dumouchel et al., 2005a,b) and is summarized here only. The injection system is a simplified cavity nozzle shown in Fig. 1. It is constituted of a superposition of three circular disks. The liquid enters the nozzle through disk 1, flows through the cavity disk (disk 2) and discharges through the orifice in disk 3. The drastic flow deflections imposed by the nozzle eccentricity (see Fig. 1) favors the development of a complex issuing flow structure. At the exit section, the flow shows a double swirl as well as a consistent turbulent level. Being used at low injection pressure (not greater than 5 bar) it was shown that the atomization efficiency was related to the

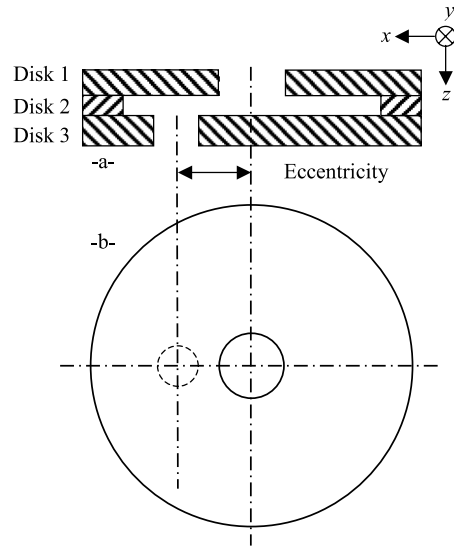


Fig. 1. The simplified compound nozzle (top: side view and coordinate system, bottom: top view).

kinetic energy of the non-axial flow component and to the turbulent kinetic energy at the nozzle exit (Dumouchel et al., 2005a). Furthermore, the low Weber numbers of the issuing flow due to the use of low injection pressures indicate the negligible role of the aerodynamic forces on the atomization process that is governed by surface tension forces only.

In the present investigation and contrary to the previous studies (Dumouchel et al., 2005a,b), a single nozzle is used with several liquids. Disk 1 has a thickness equal to 177 μm and a diameter hole equal to 300 μm . The cavity disk (disk 2) is 75 μm thick and the cavity diameter is equal to 2254 μm . The discharge orifice disk (disk 3) is characterized by a thickness equal to 76 μm , an orifice hole diameter equal to 180 μm and an eccentricity of 200 μm . In the previous investigation (Dumouchel et al., 2005a), this nozzle was the one that reported the greatest atomization efficiency. The liquids, whose physical properties are given in Table 1, differ mainly by their viscosity and surface tension. Each fluid is used at several injection pressures. For each experimental condition, the volume flow rate is measured and the discharge coefficient C_D is calculated. This coefficient is defined by:

$$C_D = \frac{Q_v}{S \sqrt{\frac{2\Delta P_i}{\rho_L}}} \quad (1)$$

where Q_v is the volume flow rate, ΔP_i the injection pressure, ρ_L the liquid density and S the area of the discharge orifice. For an injection pressure ranging from 1 bar to 5 bar, the discharge coefficient was found rather independent of the liquid and of the injection pressure. Their values are given in Table 1.

The visualization of the issuing liquid flow is performed with a Fuji Digital Camera (FinePix S1 Pro, Fuji-film, Japan) which offers a high resolution of $3040 \times 2016 \text{ pixel}^2$ and a distribution of light intensity on 256 levels for each of the three color frame components (red, green, blue). A Nanotwin Flash System (HSPS)

Table 1
Physical properties of the liquids and discharge coefficients

	ρ_L (kg/m^3)	μ (kg/m s)	σ (N/m)	C_D (-)
Water	984	$1.00 \cdot 10^{-3}$	0.0720	0.63
Heptane	704	$0.41 \cdot 10^{-3}$	0.0206	0.63
Water/glycerol (5%)	1012	$1.33 \cdot 10^{-3}$	0.0704	0.63
Water/glycerol (10%)	1030	$1.43 \cdot 10^{-3}$	0.0702	0.61

was used to enlighten the liquid flow. This light source produces short light flashes (≈ 11 ns). The light source, the liquid flow and the camera were aligned in a backlight image configuration. The light intensity was concentrated on the liquid flow by a 140 mm focal length lens. The field of visualization covered a 10.5×7 mm² area corresponding to a spatial resolution of 3.5 $\mu\text{m}/\text{pixel}$. According to the discharge coefficient and to the range of injection pressures, the maximum flowing velocity of the issuing liquid flow is of the order of 25 m/s. The corresponding displacement during the flash duration is equal to 0.25 μm . It is far less than the spatial resolution. Thus, the issuing liquid flows are well frozen. Finally, the depth of field of the imaging configuration has been measured. It is equal to 7 mm. It was reported (Dumouchel et al., 2005b) that the flow issuing from the nozzle does not keep the axisymmetry of the discharge orifice but spreads in the $(0, x, z)$ plane (see Fig. 1 for coordinate system) and that the disintegration process is organized in this plane. In the following, flows are visualized and analyzed in this plane only. Thanks to this configuration, the depth of the flow is less than the image depth of field. Thus, all the flow structures are visualized with a good contrast. This can be seen in Fig. 2 that shows examples of visualizations obtained for an injection pressure of 3.5 bar for the four liquids.

The fractal analysis we intend to perform concerns the continuous liquid flow only. Detached droplets and ligaments are not taken into account and are removed from the image. The analyzing technique to detect the continuous flow contour from the images was improved compared to the previous investigation (Dumouchel et al., 2005b). It was conducted on the blue frame of the images since its 256 gray level distribution reported the largest dynamics. This distribution showed a main peak corresponding to the background pixel population. The liquid-pixel gray-level distribution covers the all level dynamics because of light scattering effects. A double-threshold technique was applied to dissociate liquid and background pixels. Two thresholds are

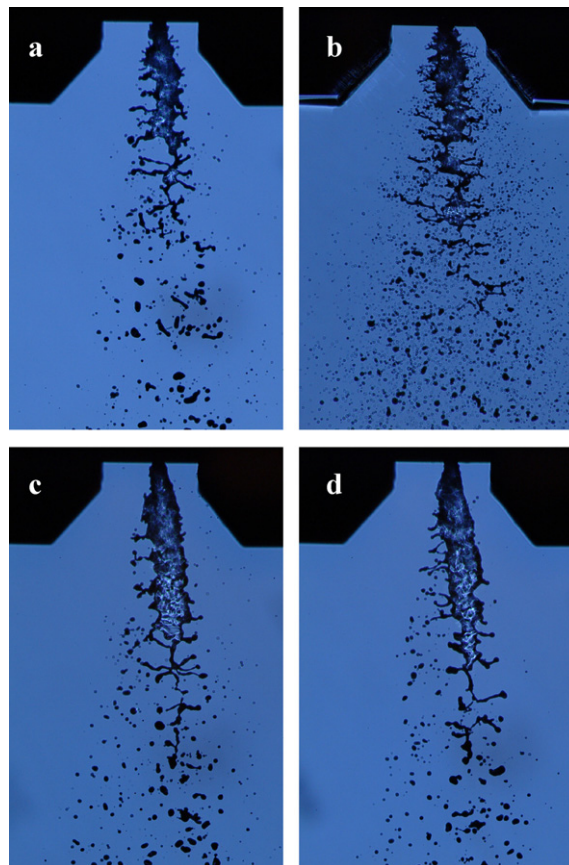


Fig. 2. Examples of liquid flow images ($\Delta P_i = 3.5$ bar, a, water; b, heptane; c, water–glycerol 5%; d, water–glycerol 10%).

selected on each side of the gray-level distribution main-peak: gray levels between these thresholds represent background pixels and are attributed the level 255 (white), the others represent liquid pixels and are attributed the level 0 (black). The good contrast of the images ensured a limited influence of the thresholds of the liquid–gas interface determination. An example of application of the double threshold technique is shown in Fig. 3. Fig. 3a shows the initial image (detail) and Fig. 3b the corresponding two-gray level image obtained after the double threshold technique. However, it can be noticed that a non-negligible amount of liquid pixels have been interpreted as background ones. This problem is mainly observed at the bottom of the continuous liquid flows where thin liquid lamella are present. These pixels increase the amount of liquid–gas interface (see Fig. 3b) and the corresponding external boundary of the liquid flow shows additional and pretty tortuous contour (see Fig. 3c). This additional contour might affect the fractal analysis and it was minimized by applying a dilation-erosion step before the contour detection.

The dilation-erosion is a two step procedure. First, a dilation of the object is performed on the two gray level image (Fig. 3b). This step consists in replacing each white pixel with at least one black neighbor by a black pixel. Each gap that is one or two pixels wide is filled. Second, an erosion step is applied to compensate the influence of the dilation on the external liquid flow boundary. This step consists in replacing each black pixel with at least one white neighbor by a white one. This does not reopen the small gaps filled during the dilation step. The result of the dilation-erosion step is illustrated in Fig. 3d and e that show the two-gray level image and the corresponding external contour, respectively. This example illustrates to which extent the problem of additional external interface creation is reduced.

The final step of the image analysis is the external contour detection. Foroutan-pour et al. (1999) recommended that fractal analysis should be conducted on skeletal images. This recommendation has been followed and will be discussed later.

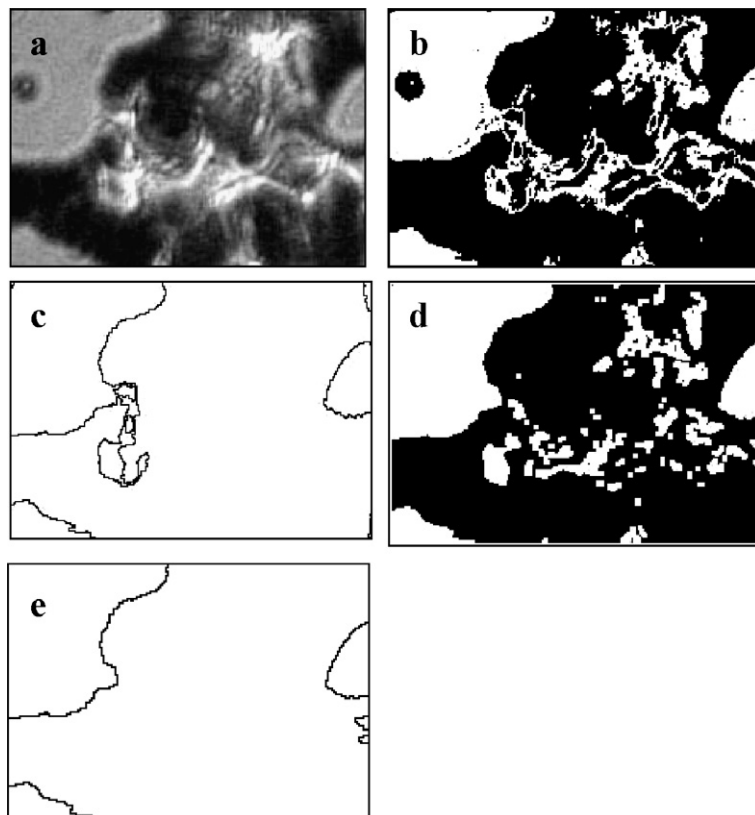


Fig. 3. Illustration of the extra contour detection due to light transmission and of the improvement due to the dilation-erosion step (a, initial image; b, binarized image; c, contour detection from image b, d, application of the dilation-erosion step on image b, e, contour detection from image d).

As done in previous investigations (Shavit and Chigier, 1995; Dumouchel et al., 2005b), we are interested in the determination of the local fractal dimension in order to investigate its evolution from the nozzle exit to the end of the primary atomization process. To achieve this, the fractal dimension was determined on portions of the liquid flow delimited by an analyzing window that is 256 pixels in height (896 μm) and as wide as the image. Thus, the objects we want to analyze are contour parts more or less close to each other according to the distance from the nozzle. They are very different to the objects analyzed in all the studies enumerated in the previous section and which were closed contours. Thus, before conducting the fractal analysis, three fractal methods were tested on synthetic images of “open” mathematical objects. This is presented in the next section.

4. Tests of fractal analysis methods

Three fractal analysis methods were tested; the minimum grid counting method (MGC), the Euclidean distance mapping method (EDM) and the mass method (MM). These techniques are introduced in Appendix A. They report a different Richardson–Mandelbrot plot as illustrated in Fig. 4 for a natural fractal object with a fractal dimension equal to δ in the range of cutoff scales $[r_{\text{inn}}; r_{\text{out}}]$. Within this scale interval, the slope of the Richardson–Mandelbrot plot is a function of the fractal dimension and of the method used (see Eqs. ((A.1)–(A.3))). Thus, the determination of the fractal dimensions requires the identification of the linear regions in the Richardson–Mandelbrot plot. In the present work, the local slope graph technique introduced by Panico and Sterling (1995) is used. It consists in calculating linear regression over a window containing a limited number of consecutive points in the Richardson–Mandelbrot plot and in plotting the local slope as the window slides over the entire scale range. If no region with a constant local slope is reported, the object is not fractal. In the present work, local linear regression are performed over seven consecutive points in the Richardson–Mandelbrot plot. As noted by Panico and Sterling (1995), we observed that smaller intervals for local slope calculation increased the noise but did not affect the apparent linearity in Richardson–Mandelbrot plots. In order to facilitate the comparison between the three methods, the local slope plot reports the corresponding local fractal dimension. This is illustrated in Fig. 5 that shows the local slope graph corresponding to the three Richardson–Mandelbrot plots presented in Fig. 4.

The three fractal analyzing methods were tested for the set of synthetic images shown in Fig. 6. These images have the same size of the analyzing window that will be used to apply local fractal analysis on the liquid flow contour, i.e. $257 \times 2016 \text{ pixel}^2$. Each image contains one or two portions of a mathematical line with known fractal properties. Image 1 contains a single vertical straight line positioned in the middle of the image.

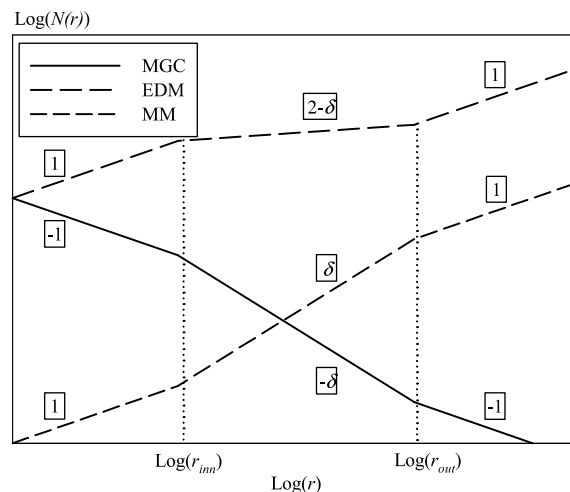


Fig. 4. Richardson–Mandelbrot plots of a natural fractal with scale similarity between r_{inn} and r_{out} as a function of the method (local slope are indicated in the squares).

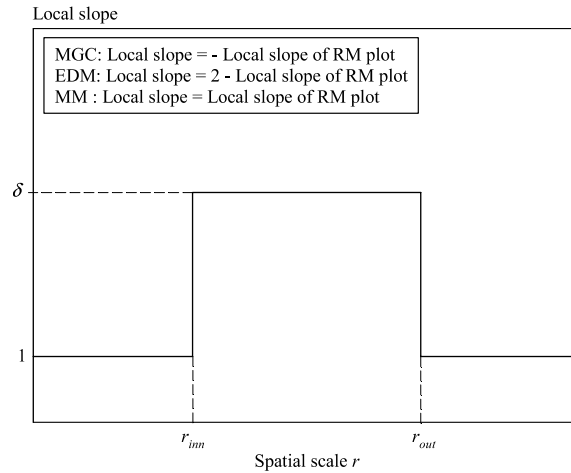


Fig. 5. The local slope graph for a natural fractal whose Richardson–Mandelbrot plots are shown in Fig. 4.

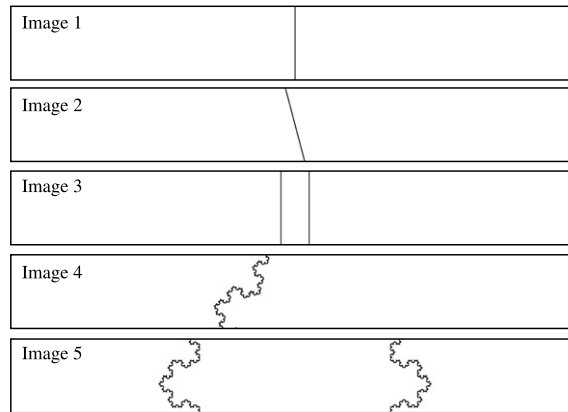


Fig. 6. The synthetic images.

The fractal dimension of this object is 1. Image 2 is an inclined single straight line with an inclination angle of 15°. The fractal dimension of this object is also equal to 1. However, the analysis of Image 2 will quantify image digitalization effect. Image 3 contains two parallel straight lines. The distance between the two lines is equal to 100 pixels. The analysis of this image will illustrate the influence of the presence of two contour portions on the determination of the fractal dimension. Image 4 contains a portion of a 5-order triadic Koch coast line. The Koch line is a linear (or ideal) fractal often used in the literature to test fractal methods (Bérubé and Jébrak, 1999; Guessasma et al., 2003; Panico and Sterling, 1995; Smith et al., 1996). It results from an absolute generating process with a known construction rule. Its fractal dimension is analytical and close to 1.2618. The portion of Koch coast line in Image 4 is inclined. Finally, Image 5 contains two portions of a 5-order triadic Koch coast line.

The three fractal methods described in Appendix A are applied on the synthetic images. For the MGC method, the size r of the square elements varies from 1 to 257 pixels, and the EDM method is applied with an interval of brightness level r ranging from 1 to 128 pixels. The MM method is local and requires defining contour pixels as centering sites. It is important that the size r of the structuring element varies in the same interval for each pixel centering site. To satisfy this requirement, the centering sites are the pixels of the contour intercepting the middle line of the analyzing window and the square size varies from 1 to 257 pixels, taking only the odd values to make sure that the centering sites is always the middle point of the square. The symmetry of Images 1, 2 and 3 renders unnecessary a statistical approach and the three methods are applied

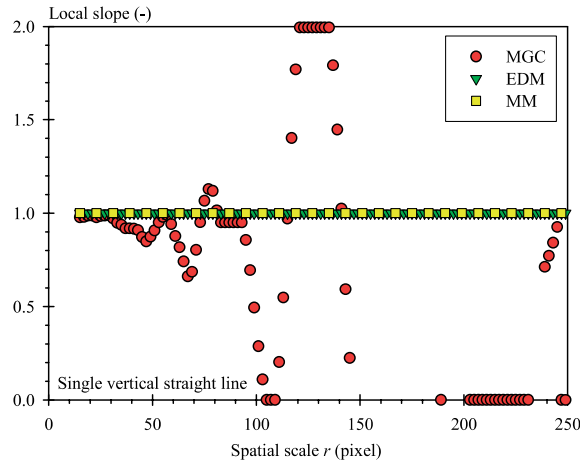


Fig. 7. Local slope graphs of Image 1 obtained with the three fractal methods.

on a single image each time. However, they are applied on 150 images for Images 4 and 5, each image showing a different part of the Koch coast line but equivalent in size. The Richardson–Mandelbrot graphs are plotted with the average of the numbers $N(r)$ obtained for each image.

Fig. 7 shows the local slope graphs obtained with the three methods for Image 1. It can be seen that over the whole spatial scale range both the EDM and MM report a constant local slope equal to 1. Bearing in mind how the local slope graph is built (see Fig. 5), this result shows that both methods find the correct fractal dimension. However, the result reported by the MGC method is drastically different. For spatial scales less than 30 pixels, the local slope is constant and equal to the expected fractal dimension 1. Above this length scale, the local slope reported by the MGC shows large and unorganized variations. This pejorative behavior is due to a scale range of the grid square elements inappropriate to the size of the image. Indeed, Foroutan-pour et al. (1999) recommended that the maximum box size in box counting methods should not exceed 25% of the smallest size of the image. If not very poor information is returned by the method. The results obtained for the other synthetic images confirm the poor appropriateness of the MGC method for the type of images analyzed in the present work. Thus, results presented in the following concentrate on the two other methods only.

Fig. 8 presents the Image 2 local slope graphs obtained with EDM and MM. This figure shows that the MM method is not at all affected by the digitalization of the object whereas it slightly modifies the result

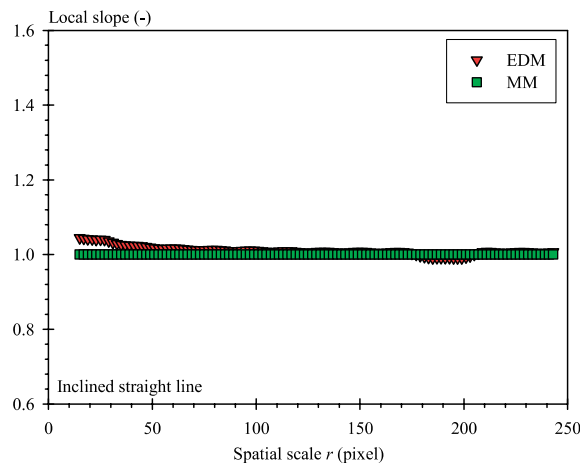


Fig. 8. Local slope graphs of Image 2 obtained with EDM and MM.

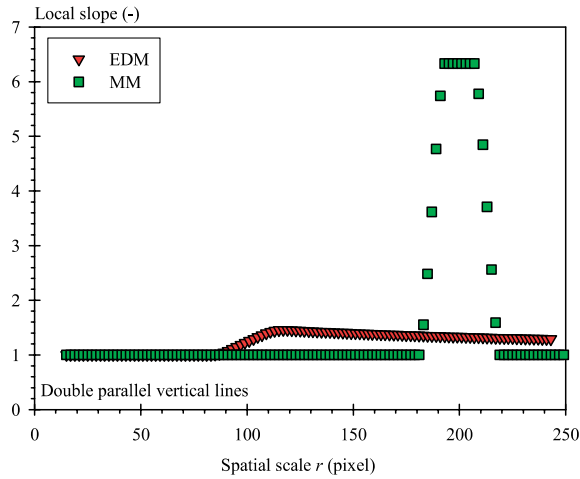


Fig. 9. Local slope graphs of Image 3 obtained with EDM and MM.

returned by EDM. This is mainly observable at small spatial scales where digitalization is interpreted as tortuosity. Thus, the fractal dimension is overestimated in this region. However, the EDM method globally reports a very acceptable value of the fractal dimension if the behavior at very small spatial scales is disregarded. Fig. 9 shows the Image 3 local slope graphs reported by EDM and MM. For both methods, the presence of two contour portions has a similar effect, which is an increase of the local slope at a given spatial scale that depends on the method. When the image is analyzed at small scales, both lines are independently analyzed and both methods report a fractal dimension equal to 1. However, at a given spatial scale r , the two line portions are seen as a single object inducing a sudden increase of the number $N(r)$ and, consequently, of the local slope. Since the two lines are 100 pixels apart, this increase is observed at $r = 100$ pixels and 200 pixels for EDM and MM, respectively. This difference is directly related to the definition of the scale r for each method (see Eqs. (A.2) and (A.3)). For larger scales, the MM local slope goes back to the value of 1. The width and height of the MM local slope peak reported in Fig. 9 are functions of the point interval used for the local slope calculation and are not physically relevant. For large scales the EDM local slope keeps an almost constant value suggesting the existence of a fractal dimension greater than 1 for this range of scales. This fractal dimension is physically meaningful and characterizes the structure of the object made of two parallel line portions

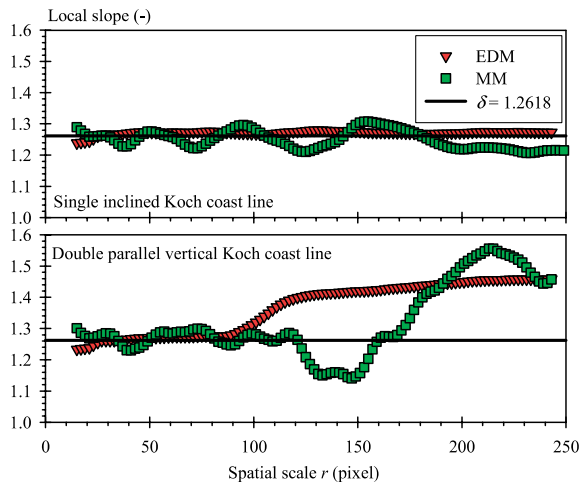


Fig. 10. Local slope graphs of Image 4 (top) and Image 5 (bottom) obtained with EDM and MM.

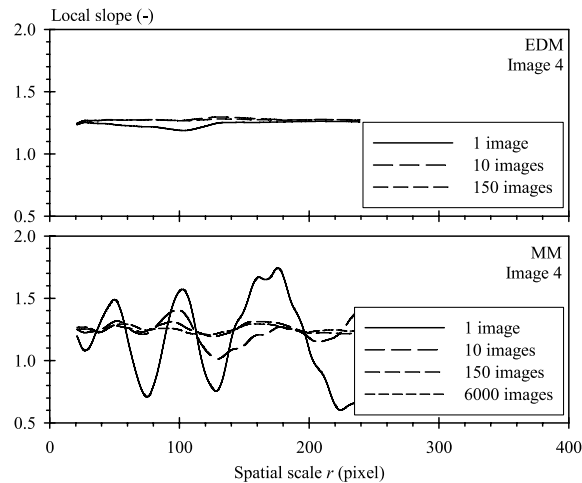


Fig. 11. Influence of the number of images on the local slope graphs for Image 4 obtained with EDM (top) and MM (bottom).

and that has a certain spatial covering capacity. Thus, contrary to the MM, EDM characterizes an object by its textural and structural fractal dimensions as defined by Kaye (1989) and introduced in the previous section.

Finally, the results obtained for Images 4 and 5 are presented in Fig. 10. As explained above, the local slope graphs for these images result from the analysis of 150 images of different portions of the Koch coast line. For the single Koch coast line portion (top of Fig. 10), the results show the very good behavior of EDM that returns a fractal dimension equal to the expected value of 1.26 constant over the whole spatial scale range. The result provided by the MM does not report a constant local slope whatever the scale range and suggests that the contour in Image 4 is not fractal, which is incorrect. The results obtained from the analysis of the double Koch coast line (bottom of Fig. 10) lead to similar conclusions. For spatial scales lower than 100 pixels, which corresponds to the smallest distance between the two lines, EDM reports a constant local slope that is equal to the fractal dimension of the contour. For greater spatial scales, EDM reports a greater constant local slope characterizing the structure of the whole object. Whatever the range of spatial scales, the MM does not return such information and appears inappropriate.

The pejorative behavior of MM compared to EDM can be understood as follows. EDM analyzes the whole contour in the image at the same time whereas MM performs a local analysis on a limited number of pixels those used as centering sites. To improve the MM performance, one has to increase the number of centering sites by increasing the number of images. This is illustrated in Fig. 11 that compares EDM and MM local slope graphs obtained for several sets of Image 4. It can be seen in this figure that the number of images considerably influences the results returned by MM, which is not the case for EDM. Indeed, the result obtained from the analysis of 6000 images with MM is not better than the one obtained from the analysis of a single image with EDM. Thus, the use of MM is definitely not appropriate to analyze liquid flow contours because of the excessive number of images it requires. On the other hand, it is interesting to note that EDM gives an acceptable result even from the analysis of a single image. This characteristic feature of this technique is used in the analysis of atomizing liquid flow contours presented in the next section.

5. Application to atomizing liquid flows

In Fig. 12, an example of the analysis of a single image is presented (water, $\Delta P_i = 4$ bar). The figure shows the image and its contour where the top short-dash rectangle schematizes the analyzing window (AW) that delimits contour portions to be analyzed by EDM. The AW has the same dimension as the synthetic images and its position is noticed by the distance h between the nozzle exit plane and the AW middle line. During the analysis, the AW is slid from the top of the liquid flow ($h = 0.7$ mm) to the distance $h = h_{BU}$ corresponding to

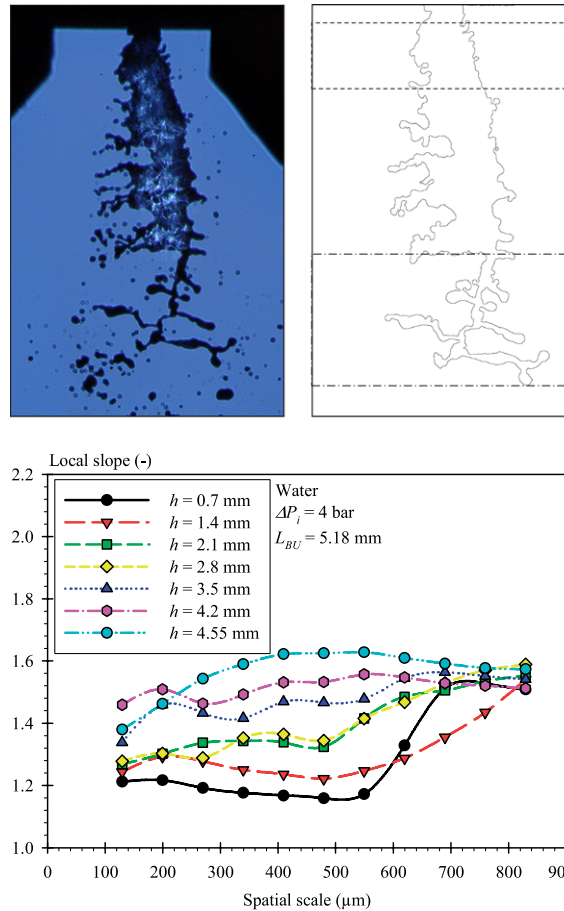


Fig. 12. Image of water flow at $\Delta P_1 = 4$ bar (top right) and corresponding contour (top left: the short-dash rectangle indicates the 257 pixels AW positioned at $h = 0.7$ mm and the dash-point rectangle indicates the 512 pixels AW positioned at $h = h_{BU}$) and the local slope graphs as a function of the AW position (bottom).

the position where the contour pixel farthest from the nozzle lies on the bottom line of AW. h_{BU} varies from one image to another.

Fig. 12 reports the EDM local slope graphs obtained at several positions h . These graphs show a clear evolution with the distance from the nozzle with constant local slopes allowing the definition of local fractal characteristics. Near the nozzle, ($h = 0.7$ mm and 1.4 mm) a textural fractal dimension is obtained in the scale range $[250 \mu\text{m}, 550 \mu\text{m}]$. For greater spatial scales, the local slope increases due to the presence of the two contours and goes toward the description of the structure of the whole liquid flow. For intermediate distances ($h = 2.1$ mm and 2.8 mm), the local slope graphs show two regions of constant value: one corresponds to the local textural fractal dimension and the other one to the local structural fractal dimension. Finally, for the greatest distances, the local slope increases and reaches a constant value for spatial scale greater than $400 \mu\text{m}$. The corresponding fractal dimension characterizes the structure of the flow that has reorganized as a ligament network at this stage.

The general behavior described by the local slope graph shown in Fig. 12 is the following. As soon as the liquid issues from the nozzle, the flow begins to distort but deformations are localized on the flow boundary only and have small characteristic spatial scales. These initial deformations are described by a local textural fractal dimension. After this first step, important deformations of the bulk flow appear with production of liquid gulfs and ligaments. At this stage, the deformations of the flow boundary and of the whole flow are described by a textural and a structural fractal dimensions, respectively. Finally, due to vivid action of surface

tension forces, the bulk flow reorganizes as a network of ligaments with rather smooth boundaries. This final liquid shape is described by a structural fractal dimension. The increase of the local textural fractal dimension in the first and middle regions and of the local structural fractal dimension in the middle and last flow distortion regions are representative of the increase of local interface surface area due to deformation growths. Furthermore, the spatial evolution of each fractal dimension spatial scale range gives information on the perturbation length scales that dominates the flow distortion process.

The results shown in Fig. 12 confirm also that atomizing liquid flows are fractal objects. This does not necessarily mean that liquid atomization is a fractal process. This latter statement would require constant local fractal characteristics during the process. To study this point, the same analysis as the one shown in Fig. 12 was performed on a series of 150 images. For each image, the textural fractal dimension near the nozzle ($h = 0.7$ mm) and the structural fractal dimension of the ligament network in the last flow distortion region ($h = h_{BU}$) were measured. For the measurement of the structural fractal dimension the AW was enlarged up to 512 pixels (1.79 mm) in order to embrace all the ligament network. This AW is shown in the contour in Fig. 12 (dot-dash box at h_{BU}). For each image, the textural fractal dimension was measured as the average of the local slope in the spatial scale range [250 μ m; 430 μ m] and the structural fractal dimension was determined as the average of the local slope in the spatial scale range [390 μ m; 700 μ m]. These measurements are reported in Fig. 13 that shows the textural and structural fractal dimension distributions. Both distributions display a rather Gaussian shape. As explained by Smith et al. (1996) the width of these distributions is partly a consequence of the use of finite digitized images that introduces fractal dimension variation. Furthermore, in the present work, it is believed that these widths are also overestimated by the experimental protocol. First, to reduce the analysis time, each fractal dimension was determined as an averaged local slope over a constant spatial scale range. However, the intermittent character of liquid atomization because of the role of turbulence, probably modifies this range from one image to another. Second, the use of a constant AW height for the measurement of the structural fractal dimension is also a source of error. The ligament network does not have the same size from one image to another and might not even be connected to the continuous liquid flow in some images. A preliminary sort of the images would have reported narrower distribution. However, the Gaussian shape of both distributions reported in Fig. 13 leads to the conclusion that liquid atomization can be considered as a fractal process and, most of all, that average fractal dimensions are relevant and should be physically representative. To emphasize this point, local average fractal dimensions were studied as a function of other liquid flow characteristics.

Average textural fractal dimensions δ_T at the nozzle exit were measured for all the fluids tested at several injection pressures. These measurements are presented in Fig. 14 as a function of the issuing liquid flow

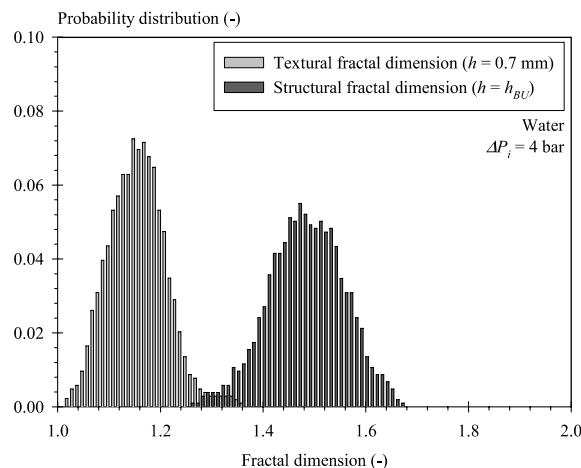


Fig. 13. Probability distributions of the initial textural fractal dimension and of the ligament network structural dimension (Water, $\Delta P_i = 4$ bar).

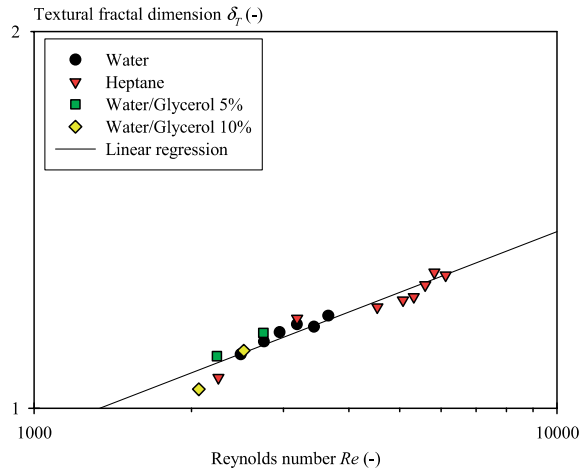


Fig. 14. Correlation between the textural fractal dimension measured at $h = 0.7$ mm and the issuing flow Reynolds number (all fluids, all injection pressures).

Reynolds number Re based on the discharge orifice diameter and on the issuing mean velocity. Whatever the working conditions, Fig. 14 shows a single correlation between δ_T and Re of the form:

$$\delta_T \propto Re^{0.16} \tag{2}$$

As found in previous investigations (Dumouchel et al., 2005a,b), the initial liquid flow deformation is due to the liquid flow turbulent level that is mostly represented by the Reynolds number. Fig. 14 confirms this finding and shows the physical relevance of the initial textural fractal dimension δ_T . Furthermore, the increase on δ_T with Re demonstrates that an increase of turbulence favors greater interface tortuosity and area production.

Similarly, average structural fractal dimensions δ_S of the ligament network were also measured. They are plotted in Fig. 15 as a function of the liquid Weber number We_L of the flow based on the liquid density, the discharge orifice diameter and the issuing mean velocity. Once again, a single correlation between δ_S and We_L is obtained:

$$\delta_S \propto We_L^{0.04} \tag{3}$$

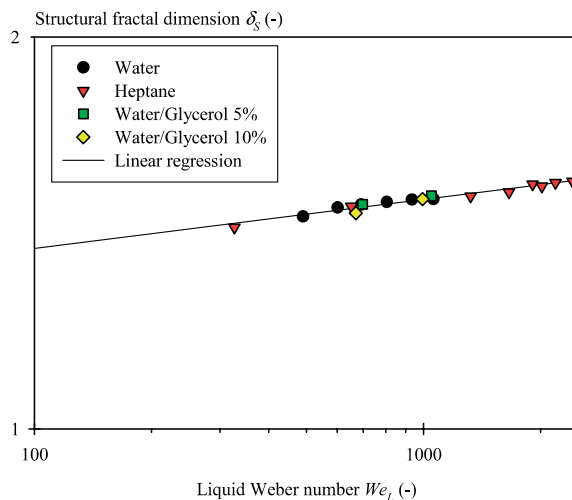
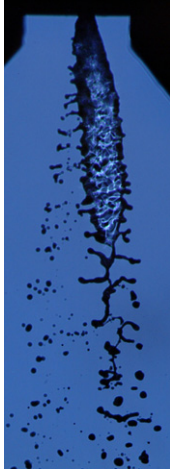
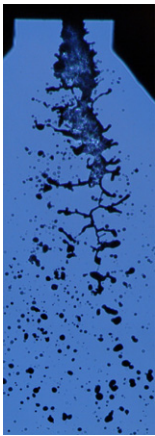
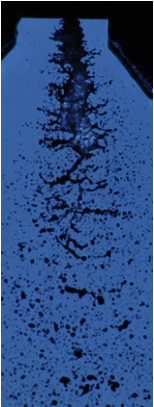


Fig. 15. Correlation between the structural fractal dimension of the ligament network and the liquid Weber number (all fluids, all injection pressures).

Table 2

Examples of atomization patterns for the ranges of Reynolds and liquid Weber numbers covered in the present study

Visualizations			
$Re(-)/\delta_T(-)$	2065/1.05	3653/1.20	6125/1.28
$We_L(-)/\delta_S(-)$	670/1.45	1061/1.49	2417/1.53

As said above, the gaseous Weber number of the liquid flow is small enough to expect the flow distortion to be governed by surface tension forces only. Thus, the structural fractal dimension that characterizes the final liquid flow shape is a unique function of a parameter representative of surface tension effects like the liquid Weber number.

To enhance the relevance of δ_T and δ_S it is interesting to note that the atomizing liquid flow report rather different patterns for the working conditions covered in this study. This is illustrated in Table 2 where visualizations for small, intermediate and large values of Reynolds and liquid Weber numbers are shown.

These results show that the fractal dimensions measured by EDM are appropriate characteristics to describe the complex shape of atomizing liquid flows. However, the information brought by fractal dimensions is qualitative and will never be sufficient to fully study and predict primary atomization processes. Quantitative information such as characteristic length scales of deformation are required if the objective is to determine information related to drop size distribution. It is believed that a fractal analysis can bring such information. To illustrate this, we consider the inner cutoff scale r_{inn} of the textural-deformation scale-range of the liquid flow just after the nozzle exit. As shown in Fig. 12, this scale increases when the distance from the nozzle increases up to $h = 2.1$ mm. As a first approximation r_{inn} was estimated as the smallest scale at which the local slope equals the average local textural fractal dimension δ_T . This estimation was performed as a function of the fluid and the injection pressure and for a distance h ranging from 0.7 mm to 2.1 mm. To study the relevance of this scale, it was compared to a typical surface-tension length-scale a_σ introduced by Dumouchel et al. (2005b) and defined as follows. For a liquid ligament characterized by a length scale a_σ and subject to a capillary instability, the characteristic break-up time t_σ is given by Rayleigh (1879):

$$t_\sigma = \frac{1}{0.343} \sqrt{\frac{\rho_L a_\sigma^3}{\sigma}} \quad (4)$$

Equating this time to the time t elapsed from the beginning of the injection allows the greatest scale controlled by surface-tension forces to be estimated. Since this analysis is limited to the first millimeters downstream the nozzle, the elapsed time t can be calculated by:

$$t = \frac{h}{V_q} \quad (5)$$

which leads to the following expression for the greatest scale controlled by surface tension forces:

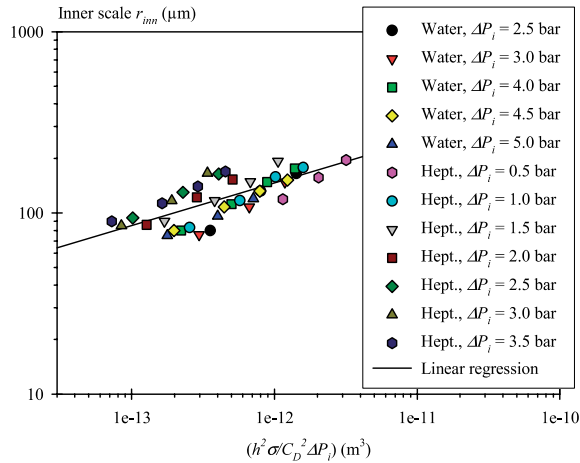


Fig. 16. Correlation between the inner cutoff scale and the cubic of surface tension characteristic length scale.

$$a_\sigma \propto \left(\frac{h^2 \sigma}{\rho_L V_q^2} \right)^{1/3} = \left(\frac{h^2 \sigma}{C_D^2 \Delta P_i} \right)^{1/3} \tag{6}$$

Fig. 16 shows the measured r_{inn} versus the distance h (expressed as $(h^2 \sigma / C_D^2 \Delta P_i)$) for water and heptane at several injection pressures. All points gather as a unique behavior. Considering the rather wide variations of surface tension and injection pressure as well as the unsophisticated procedure to estimate r_{inn} , the result shown in Fig. 16 is rather convincing all the more so since the slope of the mean regression line shown in the figure is equal to 0.23, which is of the same order of magnitude as the exponent 1/3 given by Eq. (6). Thus, the inner scale determined thanks to the fractal analysis corresponds to a surface tension characteristic length scale. This result suggests us to define the following non-dimensional group D_σ by:

$$D_\sigma = \left(\frac{r_{inn}^3 C_D^2 \Delta P_i}{h^2 \sigma} \right)^{1/3} \tag{7}$$

For all the cases shown in Fig. 16, D_σ was calculated. It is presented in Fig. 17 as a function of the distance h from the nozzle. It is interesting to note that for each working condition, this number is constant during the first stage of the atomization process. Furthermore, it can be seen that the points do not scatter that much

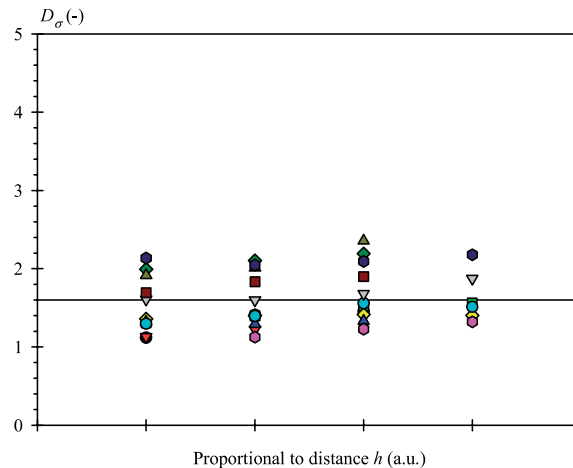


Fig. 17. Evolution of the number D_σ (Eq. (6)) with the distance from the nozzle (same legend as in Fig. 16).

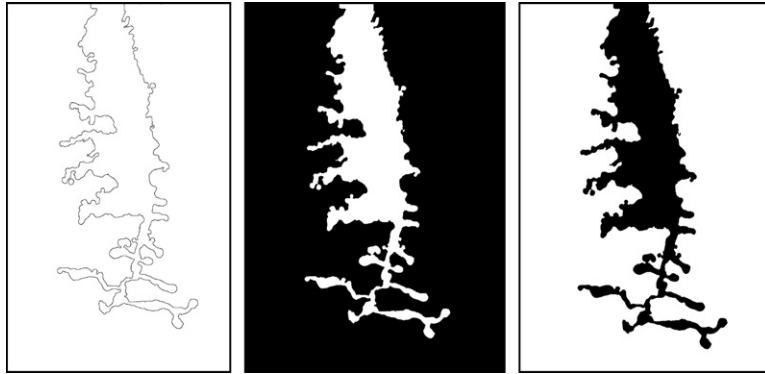


Fig. 18. The three representation modes of the same object (left: contour image, middle: silhouette image, right: shadow image).

around the mean value of D_σ equal to 1.6. Thus, the number D_σ allows the smallest perturbation scale to be estimated at the beginning of the atomization process. Eq. (7) indicates that this scale increases when the surface-tension or the distance increases or when the injection pressure decreases. This result shows to which extend fractal analysis of primary atomization process could provide physical insights for model development.

The results presented so far show that fractal analysis can be a powerful approach to analyze and study primary liquid atomization. However, it must be kept in mind that preliminary investigations are required to define the best possible protocol. Experimental aspects concerning the image generation must be considered as well as methodological aspects as far as image analyzing technique and fractal analysis method are concerned. Among the option related to the fractal analysis step, the one concerning the best object representation mode is worth to be discussed. Following Foroutan-pour et al. (1999) suggestion, the contour of the object was analyzed in the present approach. Two other alternatives are available: the silhouette and shadow representation modes. The three possible modes of representation are shown in Fig. 18. The application of EDM on these three representation modes does not lead to the same result since EDM analyses the part of the image covered by white pixels only. An example of the results obtained as a function of the representation mode is displayed in Fig. 19. This figure reports the local slope graphs for the three images shown in Fig. 18 with the AW positioned at $h = 0.7$ mm. It can be observed that although the three graphs report similar behavior in the small spatial scale range, very different results are obtained in the great spatial scale range. This difference comes from the fact that the system that is analyzed depends on the representation mode. When using the contour image, EDM is unable to dissociate liquid structure scales from gaseous structure ones. The result

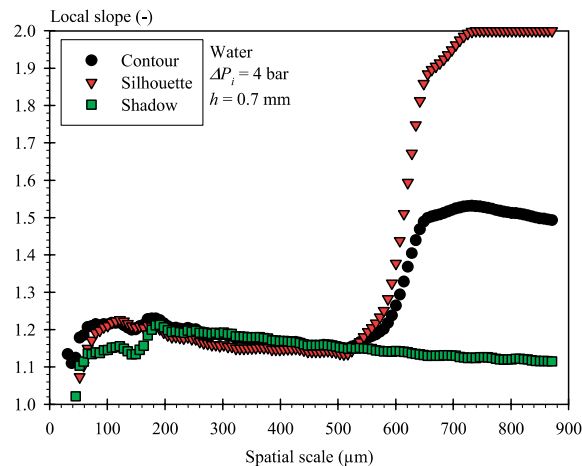


Fig. 19. Local slope graphs for the three representation modes shown in Fig. 18 ($h = 0.7$ mm).

provided by the contour analysis is a function of the liquid structure density in the gaseous environment. From this point of view the application of EDM on contour can be seen as “two-fluid” shape analysis. On the other hand, the use of the two other representation modes can be seen as “single-fluid” shape analyses. The use of silhouette images gives information on the liquid system only whereas analysis of shadow images describes the gaseous boundary only. It can be seen in Fig. 19 that within the small spatial scale range ($<500 \mu\text{m}$) the analyses of the three images give similar local slope graphs. This indicates a similitude of the deformations seen from either side of the boundary. In other words, scales of the liquid deformations are of the same order of magnitude as the scales between liquid deformations.

Fig. 19 shows however that within the large spatial scale range a sharp increase of the local slope is found from the contour and silhouette analyses, behavior that is not reported from the analysis of the shadow image. When the observation scale increases on the shadow image, the tortuosity of the gaseous boundary is less and less space covering inducing a continuous decrease of the local slope. For the two other representation modes that depend on the liquid flow, the local slope increases when the observation scale is of the order of the flow width. With the contour image, the increase lasts until the local slope reaches a rather constant value of the order of 1.5 here. As mentioned earlier, this value corresponds to the structural fractal dimension of the liquid flow and gives information on its propensity to fill space. However, the increase found from the silhouette image does not stop until the limit value of 2 is reached. This is a characteristic feature of the use of such image. The spatial scale for which the local slope is 2 is the minimum scale required to cover the entire surface represented by the liquid flow. This scale is a function of the shape of the flow. Indeed, the more elongated the flow, the smaller this minimum scale. Therefore, silhouette image analysis gives information on the spatial scale distribution that composes the liquid flow shape.

Fig. 20 presents another comparison of the local slope graphs according to the object representation mode. It corresponds to the analyses of the images shown in Fig. 18 but with $h = h_{BU}$. It is interesting to note that as far as the analysis of the ligament network is concerned, the three approaches lead to different results even within the small spatial scale range. As it can be noted in Fig. 18, small spatial scales are much more present in the liquid medium than in the gaseous one. Finally, it can also be noted in Figs. 19 and 20 that the results obtained from the analysis of the contour mode is always comprises between those obtained from the analyses of the two other modes. Therefore, the use of contour images is a more complete approach since it gives information on the spatial scale distribution in the liquid flow as well as on the spatial scale distribution between the liquid structures in the gaseous medium. This last point is in connection with what the spatial density of the spray will be. However, although the information reported by contour image analysis is complete, it is difficult to be dissociated and it is believed that, as a first approach, the analysis of silhouette images may bring very informative results especially if spray drop-size distribution wants to be determined without any consideration on spray density.

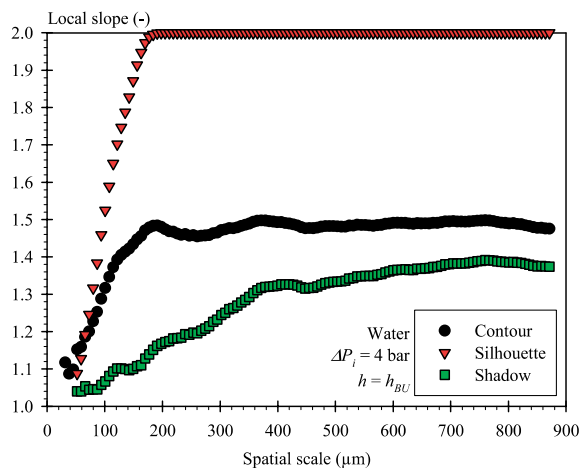


Fig. 20. Local slope graphs for the three representation modes shown in Fig. 18 ($h = h_{BU}$).

6. Conclusion

One of the most important conclusions of the work reported in this paper is that the relevance of the use of fractal concept to study liquid primary atomization process has been demonstrated. Many factors explain the appropriateness of this approach.

A fractal analysis consists in studying the shape of objects that can be achieved only if accurate images can be caught. The advantage of the present target application is that two-phase flow images with a great contrast can be achieved by using a backlight configuration set-up. Images with good contrast are required to expect the success of a fractal analysis. This ensures a wide fractal thickness in terms of gray levels and an image binarization step less influenced by the choice of the thresholds. Image contrast is greater if the thickness of the object is less than the thickness of the image. This condition is easily satisfied for the study of small liquid jets. A good temporal resolution also increases the image contrast. The light sources available today allow this requirement to be satisfied in a wide range of working conditions.

The disadvantage of liquid flow imaging in a backlight configuration is the presence of inappropriately deviated photons by light transmission. However, sophisticated image analyzing tools, like the dilation-erosion procedure used in the present approach, are available to minimize the pejorative influence of transmitted light on the contour detection.

Fractal approach in primary atomization investigation is also relevant because, as demonstrated here, an atomizing liquid flow is a natural fractal object and liquid atomization is a fractal process. This conclusion results from the use of an appropriate fractal analysis method, EDM, tested among three. A grid technique was found inappropriate because the limited height of the AW, whose purpose was to conduct local analysis, considerably reduces the possible grid spatial scale range towards the small scales. The Mass Method was found inappropriate because of the prohibitive number of images it requires.

EDM was definitely the best method for the present objectives. Besides the advantages already mentioned by previous workers (reliable, weakly sensitive to resolution, more isotropic) it was found that single image analysis is possible with EDM, that textural and structural information of the object is available and that this information is physically representative. For instance, it was found that the initial textural fractal dimension is a unique function of the issuing flow Reynolds number and that the final structural fractal dimension is a unique function of the liquid Weber number illustrating the dominant action of surface tension in the present situation. Furthermore, representative length scales were derived from the analysis and led to the definition of a number D_σ that is constant during the initial textural interface deformation.

Finally, by testing EDM on three representation modes of the same object, it has been emphasized that the application of this technique on contour images must be seen as a “two-fluid” shape analysis. The information it reports concerns indifferently liquid structure and gaseous structure length-scales. Although such information is related to characteristic fractal dimensions and is rather complete, it is believed that its use is complicated as the dissociation according to the phase is not possible. From this point of view, it has been found that EDM analysis conducted on what we referred here as silhouette images could provide a more usable information of the object. This “single-fluid” shape analysis reports a distribution of the spatial scales constituting the object. The advantage of such approach is that it can be easily applied on spray images reporting information on the drops regardless their spatial density.

Appendix A

This appendix introduces the three fractal analysis methods tested in this work.

A.1. Minimum grid counting method (MGC)

The MGC method is a length method deriving from the box counting method that consists in superimposing a regular grid of square elements of size r on the image, and in counting the number $N(r)$ of square elements intersecting the contour. The Richardson–Mandelbrot plot showing the number $N(r)$ as a function of the scale r under a logarithmic scale, reports a linear part satisfying the relation:

$$N(r) = Kr^{-\delta} \quad (\text{A.1})$$

where K is a constant, if the contour is fractal with the fractal dimension δ . This technique was used by Shavit and Chigier (1995). As pointed out by Foroutan-pour et al. (1999), Panico and Sterling (1995) and Dumouchel et al. (2005b), $N(r)$ depends also on the grid position. Foroutan-pour et al. (1999) noted that the strict estimation of a fractal dimension value requires the minimum box covering whereas Panico and Sterling (1995) and Dumouchel et al. (2005b) worked with numbers $N(r)$ averaged on a high number of grid positions. These two approaches leads to a different result. The influence of the grid position on $N(r)$ becomes more significant as the scale r increases. For a scale equal to 1 pixel, a single grid position exists and both techniques report the same $N(r)$ that is equal to the number of pixels constituting the contour. But for large scale the average number $N(r)$ is always greater than the minimum one and, according to Eq. (A.1), the average counting reports a smaller fractal dimension than the minimum counting. This might explain why the average counting may report fractal dimension less than 1 for contour lines barely tortuous as observed by Triballier (2003). To avoid this problem, it was decided here to use the minimum number $N(r)$ for each scale and to refer to this approach as the minimum grid counting method (MGC).

A.2. Euclidean distance mapping method (EDM)

Often classified in the sausage method, the EDM method was called the area method by Hall et al. (1992) and was used by Bérubé and Jébrak (1999) and by Chehroudi and Talley (2004). Each pixel of the image is given a gray level equal to the number of pixels corresponding to the shortest distance between this pixel and the contour. The Richardson–Mandelbrot graph plots the number $N(r)$ of pixels with a brightness less or equal to r as a function of $(2r + 1)$ in a logarithm scale. This is equivalent to measuring the area, in pixels, of a ribbon of width $2r + 1$ along the interface. The description of the fractal contour with this technique reports a linear Richardson–Mandelbrot plot with a slope function of the fractal dimension, namely:

$$N(r) = K(2r + 1)^{2-\delta} \quad (\text{A.2})$$

where K is a constant.

A.3. Mass method (MM)

The third method is the mass method (MM) described by Caserta et al. (1995), Panico and Sterling (1995) and Smith et al. (1996). A pixel belonging to the contour is chosen as a centering site. In the present approach, square boxes of size r are centered on it and the total number of black pixels $N(r)$ falling within the square is counted. The Richardson–Mandelbrot graph plots the number $N(r)$ as a function of r in a logarithm scale. For a fractal object, this plot is linear and the fractal dimension δ is given by:

$$N(r) = Kr^{\delta} \quad (\text{A.3})$$

where K is a constant. For a given object, the procedure must be repeated using each contour pixel belonging to a limited region as centering site. This region is delimited by the gyration radius (Panico and Sterling (1995), Smith et al. (1996)). The fractal dimension of the object is the average of the results obtained at each contour pixel belonging to the gyration region. In the present paper, the application of the MM is performed using as centering sites contour pixels belonging to the central pixel line of the analyzing window only but this, for a large number of images.

References

- Berntson, G.M., Stoll, P., 1997. Correcting for finite spatial y -scales of self-similarity when calculating the fractal dimensions of real-word structures. Proc. R. Soc. Lond. B 264, 1531–1537.
- Bérubé, J., Jébrak, M., 1999. High precision boundary fractal analysis for shape characterization. Comput. Geosci. 25, 1059–1071.
- Caserta, F., Eldred, W.D., Fernandez, E., Hausman, R.E., Stanford, L.R., Buldrev, S.V., Schwarzer, S., Stanley, H.E., 1995. Determination of fractal dimension of physiologically characterized neurons in two and three dimensions. J. Neurosci. Methods 56, 133–144.

- Chehroudi, B., Talley, D., 2004. The fractal geometry of round turbulent cryogenic nitrogen jets at subcritical and supercritical pressures. *Atom. Sprays* 14, 81–91.
- Chigier, N., 2005. The future of atomization and sprays. In: ILASS-Europe, 5th–7th September 2005, Orléans, France.
- Dumouchel, C., 2005. Experimental analysis of a liquid atomization process at low Weber number. In: ICHMT International Symposium, 6th–10th June 2005, Antalya, Turkey.
- Dumouchel, C., Cousin, J., Triballier, K., 2005a. On the role of the liquid flow characteristics on low Weber number atomization processes. *Exp. Fluids* 38, 637–647.
- Dumouchel, C., Cousin, J., Triballier, K., 2005b. Experimental analysis of liquid–gas interface at low Weber number: interface length and fractal dimension. *Exp. Fluids* 39, 651–666.
- Faeth, G.M., Hsiang, L.-P., Wu, P.-K., 1995. Structure and breakup properties of sprays. *Int. J. Multiphase Flow* 21, 99–127.
- Foroutan-pour, K., Dutilleul, P., Smith, D.L., 1999. Advances in the implementation of the box-counting method of fractal dimension estimation. *Appl. Math. Comput.* 105, 195–210.
- Guessasma, S., Montavon, G., Coddet, C., 2003. On the implementation of the fractal concept to quantify thermal spray deposit characteristics. *Surf. Coat. Technol.* 173, 24–38.
- Hall, M.J., Wengang Dai, Matthews, R.D., 1992. Fractal analysis of turbulent premixed flame images from SI engines. SAE Technical Paper 922242.
- Hunt, J.C.R., Vassilicos, J.C., 1991. Kolmogorov's contribution to the physical and geometrical understanding of small-scale turbulence and recent developments. *Proc. R. Soc. Lond. A* 434, 183–210.
- Kaye, B.H., 1989. *A Random Walk Through Fractal Dimensions*. VCH, New-York.
- Köylü, Ü.Ö., Faeth, G.M., Farias, T.L., Carvalho, M.G., 1995. Fractal and projected structures properties of soot aggregates. *Combust. Flame* 100, 621–633.
- Lane-Serff, G.F., 1993. Investigation of the fractal structure of jets and plumes. *JFM* 249, 521–534.
- Mandelbrot, B., 1982. *The Fractal Geometry of Nature*. WH Freeman & Co, New-York.
- Panico, J., Sterling, P., 1995. Retinal neurons and vessels are not fractal but space-filling. *J. Comp. Neurol.* 361, 479–490.
- Prasat, R.R., Sreenivasan, K.R., 1990. The measurement and interpretation of fractal dimensions of the scalar interface in turbulent flows. *Phys. Fluids*, 2, 792–807.
- Rayleigh, L., 1879. On the stability of jets. *Proc. Lond. Math. Soc.* 10, 4–13.
- Shavit, U., Chigier, N., 1995. Fractal dimensions of liquid jet interface under break-up. *Atom. Sprays* 5, 525–543.
- Sirignano, W.A., Mehring, C., 2000. Review of theory of distortion and disintegration of liquid streams. *Prog. Energy Combust. Sci.* 26, 609–655.
- Smith Jr., T.G., Lange, G.D., Marks, W.B., 1996. Fractal methods and results in cellular morphology – dimensions, lacunarity and multifractal. *J. Neurosci. Methods* 69, 123–136.
- Sreenivasan, K.R., 1991. Fractal and multifractal in fluid turbulence. *Annu. Rev. Fluid Mech.* 23, 539–600.
- Sreenivasan, K.R., Meneveau, C., 1986. The fractal facets of turbulence. *JFM* 173, 357–386.
- Triballier, K., 2003. Etude énergétique des processus d'atomisation primaire: application au comportement des injecteurs essence basse pression à triple disque. PhD, University of Rouen, France, 19th December 2003.